Defence Research and Development Canada | Recherche et développement pour la défense Canada

CAN UNCLASSIFIED

DRDC | RDDC
technologysciencetechnologie

Phased-Array Beam-Diversity with Multiple Channels for Improved SAR Imaging

Ishuwa Sikaneta
IEEE

Christoph Gierull
DRDC – Ottawa Research Centre
IEEE

IEEE Journal of Selected Topics in Applied Earth Observations and Remote Sensing

VOL. 8, NO. 11

Date of Publication from External Publisher: November 2015

Defence Research and Development Canada
External Literature (P)
DRDC-RDDC-2017-P114
November 2017

Canada

IMPORTANT INFORMATIVE STATEMENTS

This document was reviewed for Controlled Goods by Defence Research and Development Canada (DRDC) using the Schedule to the *Defence Production Act*.

Phased-Array Beam-Diversity With Multiple Channels for Improved SAR Imaging

Ishuwa Sikaneta, *Senior Member, IEEE*, and Christoph Gierull, *Senior Member, IEEE*

***Abstract*—This paper discusses the ability of a SAR to create high-resolution images with high sensitivity in a stripmap configuration. Since geometric resolution is driven by the effective azimuth beamwidth of the antenna, it compares beam spoiling methods to beam switching methods with particular attention to the achieved SNR. It also formulates the effects of element mutual coupling on the SNR. Further, since existing systems may not be able to switch beams at a rate equivalent to the PRF, this paper also discusses a method to process beam switched data collected in a burst configuration, showing that SNR and the presence of grating lobes trade against each other as the number of pulses per burst increases. Finally, this paper investigates improvements to signal quality offered by using a multichannel system, with elements aligned in the flight direction, over a single channel system.**

***Index Terms*—Ambiguity ratio, beam diversity, geometric resolution, phased array, radiometric resolution, SAR.**

I. Introduction

THE INFORMATION content of a SAR image is mainly driven by the geometric and radiometric resolution [1], [2]. While the geometric resolution specifies how far apart two scatters should be to distinguish them in an image, the radiometric resolution, or sensitivity, specifies how bright the scatterer must be to distinguish it from noise and other interference.

The geometric resolution of a SAR is a two-part quantity, with the range resolution depending on the bandwidth of the utilized pulse and the azimuth resolution dependent on the span of angles from which the target is viewed. Stripmap SAR imaging benefits from a wide antenna pattern to maximize the range of angles from which a target is viewed [2]. Spotlight SAR utilizes an antenna that is either mechanically or electronically steered to achieve an even wider range of angles without the need for a wide pattern [3]. The drawback of a Spotlight mode is that only a small area can be imaged at a time as the antenna is directed only to a single point on the ground.

The width of an antenna pattern is inversely proportional to the spatial extent, or aperture, of the antenna [1]. In stripmap modes, to generate a wide antenna pattern, a short antenna is preferred. A short antenna, especially, a short phased-array antenna, cannot support the transmission of as much power as a longer antenna, and it is the amount of power delivered to the scene that determines the radiometric resolution [1]. For instance, a large phased-array can be configured to only transmit from a small subarray to generate a wide beam. The total power conveyed by the beam is proportional to the number of element in the array that are used. The multichannel signal processing methods investigated in [4]–[8], require a wide azimuth beam to illuminate the scene and use a set of receive beams to create a high-resolution SAR image despite operating at low pulse repetition frequencies (PRFs). Although these SAR configurations can yield high geometric resolution, the wide transmit beam requirement and low PRFs can limit the amount of power transferred to the scene and can degrade the radiometric sensitivity of the measurements.

Alternatively, a large phased-array can be configured to transmit using the entire array but with electronic weightings designed to generate a spoiled beam [9]. A particular example of this is a parabolic phase weighting which generates a wide beam. The slope of the parabola at any point on the array can be considered as a local linear phase suggesting that the local set of phased-array elements generates a beam that is steered in a direction corresponding to the slope of the phase [1]. From one point to another on the array, the beam is steered over a range of angles creating a wide beam. While one can generate arbitrarily wide beams with this simple theoretical model, one encounters physical limitations when the antenna cannot efficiently transmit energy in all these simultaneous directions due to mutual coupling between array elements which changes the impedance characteristics [10], [11].

This paper introduces a new method to generate wide antenna beams with a long phased-array antenna. The method relies on time-division multiplexing of a number of different beams, each pointing in a different azimuth direction, as alluded to in [6] and discussed in [12]. The idea of multiple beams, including the concept of switching azimuth beams is also discussed in [13]. In this paper, however, the beams are nonoverlapping and disjoint in the k-space representation which precludes coherent processing for improved geometric resolution because of the large gaps between beams. The objective is to measure azimuth displacement over the time between measurement by the different azimuth beams.

As a set, the different azimuth pointing directions amount to an increased range of angles from which a target is observed. That is, the different azimuth beams populate the k-space of [14] although in a nontraditional manner. As opposed to beam spoiling, time-division increases the number of available degrees of freedom, and, as will be shown, permits more power to be reflected from a target for a given bandwidth. By operating

Manuscript received March 08, 2015; revised August 07, 2015; accepted September 08, 2015. Date of publication December 06, 2015; date of current version January 18, 2016.

I. Sikaneta is with the Radar Systems, DRDC Ottawa, Ottawa, ON K1A 0Z4, Canada (e-mail: ishuwa.tinda@gmail.com).

C. Gierull is with the Radar Systems Section, Defence Research Development Canada-Ottawa (DRDC-O), Ottawa, ON K1A 0Z4, Canada.

Color versions of one or more of the figures in this paper are available online at http://ieeexplore.ieee.org.

Digital Object Identifier 10.1109/JSTARS.2015.2483758

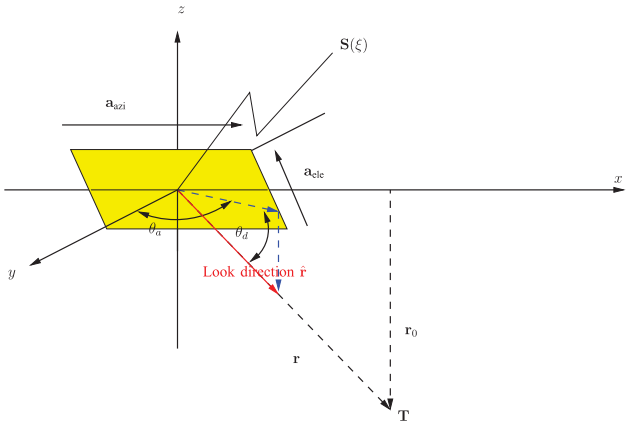

Fig. 1. Geometry of the antenna element. The $\mathbf{a}_{\text{azi}}$ axis of each antenna aligns with the direction of motion of the radar platform.

the beam switching on a periodic cycle, the collection geometry permits acquisition over long time durations as done with stripmap modes.

If the set of azimuth beams cannot be switched at the PRF, as is the case with RADARSAT-2, it may still be possible to switch them in a bursting fashion. The literature is not clear on which systems can change beams at the PRF, but it is expected that the upcoming RCM mission and most future missions will have the ability to switch beams at the PRF. The burst approach, however, introduces new grating lobes to the synthetic aperture array factor, so this paper introduces a processing approach that attempts to mitigate these new grating lobes. As the angle between beams increases, or as the number of pulses per burst increases, the ability to eliminate the new grating lobes comes at the cost of decreasing SNR; thus, this paper also introduces measurements and signal processing using a multichannel system to improve SNR while still adequately minimizing the grating lobes.

II. Power Considerations

This section analyzes the total power transmitted and received by a stripmap SAR phased array in the forward direction to motivate the time-division beam switching approach. The objective is to determine changes in power given a set of beamforming coefficients and the array mutual impedance matrix.

Assume an array of identical two-dimensional (2-D) antennas with axes given by $\{\mathbf{a}_{\text{azi}}, \mathbf{a}_{\text{ele}}\}$ as illustrated in Fig. 1. For any given "look-direction" vector $\hat{\mathbf{r}}$, the antenna radiation pattern (of each antenna element in the array) may be represented by the function $\mathcal{F}(\hat{\mathbf{r}} \cdot \mathbf{a}_{\text{azi}}, \hat{\mathbf{r}} \cdot \mathbf{a}_{\text{ele}})$. For the adopoted model, it is assumed that the $\mathbf{a}_{\text{azi}}$ axis of each antenna in the array is aligned with the x-direction, which is the direction of motion of the radar platform.[1]

In a typical SAR geometry, the radar platform has a position vector given by $\mathbf{S}(\xi)$ where ξ is the parameter, typically called slow-time. We define the x-axis as the direction of motion of the radar under the assumption that it travels in a straight line, and define the closest range vector as $\mathbf{r}_0 = \mathbf{S}(\xi_0) - \mathbf{T}$ where ξ_0 is the parameter that minimizes $J(\xi) = \|\mathbf{S}(\xi) - \mathbf{T}\|$, where, $\|\mathbf{x}\| = \sqrt{\mathbf{x}^\dagger \mathbf{x}}$, $\cdot^\dagger$ denotes Hermitian conjugate. We further make the assumption that, for the imaging geometry, the range of angles spanned by θ_d, as the SAR measures a target at a given range, is so small that it may be considered constant. For all points on the ground with a common $\mathbf{r}_0$, one may define the directional cosines

$$u = \hat{\mathbf{r}} \cdot \frac{\mathbf{a}_{\text{azi}}}{\|\mathbf{a}_{\text{azi}}\|} \tag{1}$$

$$v_{r_0} = \hat{\mathbf{r}} \cdot \frac{\mathbf{a}_{\text{ele}}}{\|\mathbf{a}_{\text{ele}}\|} = \text{Constant}. \tag{2}$$

In the far-field, u and v_{r_0} will be the same for all antennas in the array, and, for simplification of notation, define the function $\mathcal{F}_u(u) = \mathcal{F}(u, v_{r_0})$.

[1]The objective of aligning the antenna with the direction of flight is the goal of yaw-steered systems such as RADARSAT-2, TerraSAR-X and other more recently launched systems.

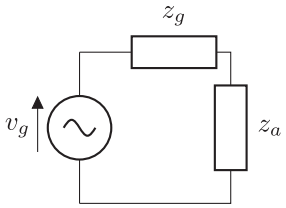

Fig. 2. Simple model for each antenna element. An alternating voltage, v_g drives the antenna element. The circuitry leading to the antenna terminal has impedance given by z_g while the antenna has a load impedance given by $z_a = R_a + \jmath X_a$ where R_a is the resistance of the load and X_a is the reactance of the load.

A. Transmitted Power

From a certain point of view, the element factor (the antenna pattern of each antenna element in the array, gain, and directivity) can be considered to depend on $\mathbf{v}$, the vector of voltages applied across the array. As the voltages are increased, the current densities increase and, as the far-field expression for the electric field is represented by the Fourier transform of the current densities, the strength of the electric field is also increased. For the simple model adopted, this dependence is computed. Assume that the mutual impedance matrix between the elements is given by

$$\mathbf{Z} = \begin{bmatrix} z_{00} & z_{01} & \cdots \\ z_{10} & z_{11} & \cdots \\ \vdots & \vdots & \ddots \end{bmatrix}. \tag{3}$$

When there is no mutual coupling between elements $\mathbf{Z} = z_a \mathbf{I}$, where $\mathbf{I}$ is the identity matrix. For each individual element, a simple representation of the circuit describing the element is given in Fig. 2.

In the case of a very large array, let us assume that the far-field element patterns are all identical and given by the three-dimensional (3-D) Fourier transforms of the current densities on the antennas. Due to mutual coupling, these currents are seen to change as the antenna is modified with the voltages $\mathbf{v}$, where

$\mathbf{v}$ is a column vector that lists the set of voltages used to drive each element of the array.

Define the array characteristic phase vector as

$$\mathbf{e}(u) = \begin{bmatrix} \exp(\jmath\beta x_0 u) \\ \vdots \\ \exp(\jmath\beta x_{N-1} u) \end{bmatrix} \tag{4}$$

with $\beta = 2\pi/\lambda$, and x_i the locations of each antenna element. The array radiation pattern is given by

$$\mathcal{F}_{T_x}(u;\mathbf{v}) = \mathcal{F}_u(u)[\underbrace{(z_g\mathbf{I}+\mathbf{Z})^{-1}}_{\mathbf{\Omega}}\mathbf{v}]^T\mathbf{e}(u) \tag{5}$$

where $\cdot^T$ represents the matrix transpose operation. The average amplitude of the electric field E_{av} in a particular direction $\{u, v_{r_0}\}$ is proportional to the array radiation pattern and inversely proportional to the range (the electric field decays at $1/r$ rate in free space) r_0 [15]

$$E_{av}(u) = C_0\frac{\mathcal{F}_{T_x}(u;\mathbf{v})}{r_0} \tag{6}$$

where C_0 is a unitless proportionality constant that incorporates such factors as the wavelength, system losses, etc. The power denisity ($\mathrm{W/m^2}$) of the transmitted wave (average value of the Poynting vector amplitude) may then be represented as

$$\rho(u, r_0) = c\epsilon_0\frac{C_0^2|\mathcal{F}_{T_x}(u;\mathbf{v})|^2}{2r_0^2} \tag{7}$$

where c is the speed of light in free space and ϵ_0 is the permitivity of vacuum. Under the assumption that the total forward transmitted power is proportional to the power transduced by the load resistance R_a of each antenna element (see Fig. 2), an expression for the total power density as the target is irradiated from $u \in [-1, 1]$ (due to the motion of the radar platform) at a range r_0, is given by

$$\begin{aligned} P(\mathbf{v}) &\propto \frac{c\epsilon_0 R_a C_0^2}{2r_0^2}\int_{-1}^{1}|\mathcal{F}_{T_x}(u;\mathbf{v})|^2\mathrm{d}u \\ &= \frac{c\epsilon_0 R_a C_0^2}{2r_0^2}[\mathbf{\Omega v}]^T\left[\int_{-1}^{1}|\mathcal{F}_u(u)|^2\mathbf{e}(u)\mathbf{e}^\dagger(u)\mathrm{d}u\right][\mathbf{\Omega v}]^* \end{aligned} \tag{8}$$

where $\cdot^*$ denotes the conjugate operation, and we have incorporated the range and other factors into the proportionality constant. This paper assumes a uniformly spaced phased array, i.e., $x_k = x_0 + kd$, where x_0 is some origin. Let

$$\begin{aligned} \mathbf{F} &= \int_{-1}^{1}|\mathcal{F}_u(u)|^2\mathbf{e}(u)\mathbf{e}^\dagger(u)\mathrm{d}u \\ &= \begin{bmatrix} F_0 & F_{-1} & F_{-2} & \dots \\ F_1 & F_0 & F_{-1} & \dots \\ F_2 & F_1 & F_0 & \dots \\ \vdots & \vdots & \vdots & \ddots \end{bmatrix} \end{aligned} \tag{9}$$

where

$$F_k = \int_{-1}^{1}|\mathcal{F}_u(u)|^2\exp(-\jmath\beta k d u)\mathrm{d}u. \tag{10}$$

The integration can be computed numerically with the desired degree of accuracy. As an alternative to this, and as argued in the appendix, for asymptotically large N, and for an antenna pattern with neglibile back lobes, $\mathbf{F}$ can be approximated as a matrix with eigenvectors given by

$$\mathbf{u}_k = \frac{1}{\sqrt{N}}\begin{bmatrix} \exp(-\jmath 2\pi k\frac{0}{N}) \\ \exp(-\jmath 2\pi k\frac{1}{N}) \\ \vdots \\ \exp(-\jmath 2\pi k\frac{N-1}{N}) \end{bmatrix} \tag{11}$$

and eigenvalues

$$\varsigma_k = \frac{\lambda}{d}\sum_m\left|\mathcal{F}_u\left(\frac{\lambda[k+mN]}{Nd}\right)\right|^2. \tag{12}$$

With these expressions, the integrated power is given by

$$P(\mathbf{v}) \propto \frac{c\epsilon_0 R_a C_0^2}{2r_0^2}\sum_{k=0}^{N-1}\varsigma_k\mathbf{u}^\dagger{}_k(z_g\mathbf{I}+\mathbf{Z})^{-1}\mathbf{v}\mathbf{v}^\dagger(z_g^*\mathbf{I}+\mathbf{Z}^\dagger)^{-1}\mathbf{u}_k. \tag{13}$$

In the particular special case of no mutual coupling ($\mathbf{Z} = z_a\mathbf{I}$)

$$P(\mathbf{v}) \propto \frac{c\epsilon_0 R_a C_0^2}{2r_0^2}\frac{1}{|z_g+z_a|^2}\sum_{k=0}^{N-1}\varsigma_k\mathbf{u}^\dagger{}_k\mathbf{v}\mathbf{v}^\dagger\mathbf{u}_k \tag{14}$$

which is maximized for a given $\|\mathbf{v}\|$ when $\mathbf{v}$ is colinear with $\mathbf{u}_0$ (because the $\mathbf{u}_k$ form an ortho-noormal basis). The above maximization depends on the assumption that ς_0 is the largest eigenvalue. In this case

$$P(\|\mathbf{v}\|\mathbf{u}_0) \propto \frac{c\epsilon_0 R_a C_0^2}{2r_0^2}\frac{\|\mathbf{v}\|^2\lambda\sum_m\|\mathcal{F}_u(m\lambda/d)|^2}{d|z_g+z_a|^2}. \tag{15}$$

The ratio of power transmitted for an arbitrary $\mathbf{v}$ relative to $\mathbf{v} = \|\mathbf{v}\|\mathbf{u}_0$ (under the assumption that there is no mutual coupling), assuming that $\|\mathbf{v}\|$ remains constant is seen to be

$$\frac{P_{\mathrm{c}}(\mathbf{v})}{P_{\mathrm{nc}}(\|\mathbf{v}\|\mathbf{u}_0)} = \frac{\sum_{k=0}^{N-1}\varsigma_k\mathbf{u}^\dagger{}_k(z_g\mathbf{I}+\mathbf{Z})^{-1}\mathbf{v}\mathbf{v}^\dagger(z_g^*\mathbf{I}+\mathbf{Z}^\dagger)^{-1}\mathbf{u}_k}{\|\mathbf{v}\|^2|z_g+z_a|^{-2}\sum_{k=0}^{N-1}\varsigma_k} \tag{16}$$

where the subscripts "c" and "nc" denote coupling and no coupling, respectively. The above expression corresponds to the result presented in [11].

B. Two-Way Power Characteristics

The received signal coming from direction u is measured by each element k of the phased array, multiplied by a receive weighting r_k and then all measurements are summed using a power combiner.

By reciprocity, the receive antenna pattern is given by

$$\mathcal{F}_{R_x}(u;\mathbf{r}) = \frac{\mathcal{F}_u(u)}{\|\mathbf{\Omega r}\|}[\mathbf{\Omega r}]^T\mathbf{e}(u) \tag{17}$$

where $\mathbf{r}$ is the column vector of r_k's. The $\|\mathbf{\Omega r}\|$ factor in the denominator serves to ensure that the receive amplitude weighting does not artificially add power; rather, it only modifies the

receive gain and directivity. The total power transmitted and received from the forward direction is then proportional to (18), shown at the bottom of the page, where A_e is the effective antenna area for each element of the array, $\sqrt{1-u^2}$ accounts for the projection of A_e into the receive direction, C_1 is another proportionality constant, and

$$\tilde{\mathcal{F}}_u(u;\mathbf{r}) = {\mathcal{F}_u}^2(u)[\mathbf{\Omega r}]^T\mathbf{e}(u)(1-u^2)^{\frac{1}{4}}. \tag{19}$$

The proportionality constant in the expression for the two-way power depends on quantities such as the range, the scattering radar cross-section (RCS) of the target and the wavelength. Exact computation of the proportionality constant is not necessary for the purpose of comparing the performance of different beams measuring the same target from a given system.

The same machinery that led to (12) yields

$$P(\mathbf{v},\mathbf{r}) \propto \frac{c\epsilon_0 R_a C_0^2 C_1^2}{2r_0^4} \frac{NA_e}{2\left\|\mathbf{\Omega r}\right\|^2} \sum_k \zeta_k \left\|[\mathbf{\Omega r}]^T\mathbf{u}_k\right\|^2 \left|[\mathbf{\Omega v}]^T\mathbf{u}_k\right|^2 \tag{20}$$

where

$$\zeta_k = \frac{\lambda}{d}\sum_m \left|\mathcal{F}_u\left(\frac{\lambda[k+mN]}{Nd}\right)\right|^4. \tag{21}$$

C. Relation to the SAR Radar Equation

It is of interest to relate the computed power to the traditional radar equation [2]. For the traditional equation, the power measured by the radar from a point target at range r_0 is given by

$$P_r = \frac{P_s G_{T_x} G_{R_x}}{(4\pi)^3 r_0^4}\frac{\lambda^2 B\tau}{L_s}\sigma \tag{22}$$

where P_s is the transmitted power, G_{T_x} and G_{R_x} are the transmit and receive gains, L_s represents system losses, λ is the radiation wavelength, B is the pulse bandwidth, τ the pulse length ($B\tau$ is the pulse compression gain), and σ is the scattering crosssection of the target.

Equation (20) incorporates the integrated transmit and receive gain and the transmitted power. The expression for the power reflected from a target is proportional to the target RCS and the compression gain of the transmitted waveform and also inversely proportional to system losses

$$\begin{aligned} P_m(\mathbf{v},\mathbf{r}) &= P(\mathbf{v},\mathbf{r})\frac{B\tau\sigma}{L_s} \\ &= B\tau\sigma\frac{c\epsilon_0 R_a C_0^2 C_1^2}{2r_0^4 L_s}\frac{NA_e}{2\left\|\mathbf{\Omega r}\right\|^2}\sum_k \zeta_k \left|[\mathbf{\Omega r}]^T\mathbf{u}_k\right|^2 \left|[\mathbf{\Omega v}]^T\mathbf{u}_k\right|^2. \end{aligned} \tag{23}$$

Since

$$A_e \propto \frac{\lambda^2}{4\pi}G_e \tag{24}$$

where G_e is the gain of each antenna element, one may write that

$$\begin{aligned} P_m(\mathbf{v},\mathbf{r}) \propto B\tau\sigma\frac{c\epsilon_0 R_a C_0^2 C_1^2}{4r_0^4 L_s}\frac{N\lambda^2}{(4\pi)\left\|\mathbf{\Omega r}\right\|^2} \\ \times \sum_k \zeta_k \left|[\mathbf{\Omega r}]^T\mathbf{u}_k\right|^2 \left|[\mathbf{\Omega v}]^T\mathbf{u}_k\right|^2. \end{aligned} \tag{25}$$

By comparing with the standard radar equation, one finds that the phased-array SAR equation relates to the power and gain of the standard radar equation through

$$\begin{aligned} \frac{P_s G_{T_x} G_{R_x}}{(4\pi)^2} = \frac{c\epsilon_0 R_a C_0^2 C_1^2}{4}\frac{N}{\left\|\mathbf{\Omega r}\right\|^2} \\ \times \sum_k \zeta_k \left|[\mathbf{\Omega r}]^T\mathbf{u}_k\right|^2 \left|[\mathbf{\Omega v}]^T\mathbf{u}_k\right|^2. \end{aligned} \tag{26}$$

1) Signal-to-Noise Ratio (SNR): With the standard radar equation, the measured signal is compromised by additive white noise with power given by

$$P_n = k_{\mathrm{B}} T B \tag{27}$$

where k_{B} is Boltzmann's constant, T is the radar temperature in Kelvin, and B is the bandwidth of the pulse. The SNR is then given by

$$\gamma_0 = \frac{P_s G_{T_x} G_{R_x}}{(4\pi)^3 r_0^4}\frac{\lambda^2\tau}{k_{\mathrm{B}} T L_s}\sigma. \tag{28}$$

The expression in (25) depends on the assumption that the reflected return from each pulse transmitted by the radar as it sweeps by the target has been added coherently with uniform weighting. Additive thermal noise is not coherent from pulse to pulse, and the total noise power interfering with the SAR measurement depends on the weightings applied as each pulse is coherently combined. The uniform weighting scheme, as assumed for the total reflected power, does not, in general, lead to an optimum SNR. In practice, the SNR yield from uniform weighting is often very undesirable. It is well known that the weightings of a matched filter optimize the SNR and, because they define the shape of the two-way antenna pattern, the optimum SNR depends on the chosen values for $\mathbf{v}$ and $\mathbf{r}$. For this reason, it is not straightforward to provide a closed-form solution for the expected SNR for a phased-array SAR, and this paper adopts the approach of comparing SNR yield by numerically computing the SNR from measurements processed with optimal weightings.

$$\begin{aligned} P(\mathbf{v},\mathbf{r}) &\propto \frac{c\epsilon_0 R_a C_0^2}{2r_0^4}\frac{A_e C_1^2}{2\left\|\mathbf{\Omega r}\right\|^2}\int_{-1}^{1}|{\mathcal{F}_u}^2(u)[\mathbf{\Omega v}]^T\mathbf{e}(u)[\mathbf{\Omega r}]^T\mathbf{e}(u)|^2\sqrt{1-u^2}\mathrm{d}u \\ &= \frac{c\epsilon_0 R_a C_0^2}{2r_0^4}\frac{A_e C_1^2}{2\left\|\mathbf{\Omega r}\right\|^2}[\mathbf{\Omega v}]^T\left[\int_{-1}^{1}|\tilde{\mathcal{F}}_u(u;\mathbf{r})|^2\mathbf{e}(u)\mathbf{e}^{\dagger}(u)\mathrm{d}u\right][\mathbf{\Omega v}]^* \end{aligned} \tag{18}$$

TABLE I
EIGHT-ELEMENT ARRAY PARAMETERS

Wavelength	$\lambda = 3.2$ cm
Elemental antenna length	$L = 8.5$ cm
Spacing	$d = 9.0$ cm
Element pattern	$\text{sinc}\left(\frac{Lu}{\lambda}\right)$
Number of elements	$N = 8$
Mutual impedance	$\mathbf{Z} = z_a\mathbf{I}$

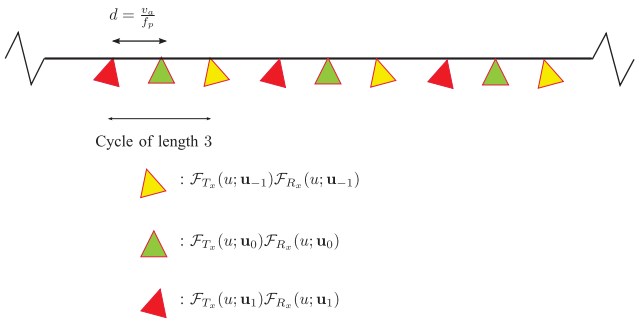

Fig. 3. Three-beam measurement approach. The two-way patterns repeat on a cycle of length three. Each beam is steered in the direction corresponding to $\{\mathbf{u}_{-1}, \mathbf{u}_0, \mathbf{u}_1\}$.

D. Simulation With Two Different Two-Way Weightings

The parameters listed in Table I are used to generate the patterns of a three-beam system and a beam-spoiled system. On a cycle of length 3, see Fig. 3, the three-beam system transmits and receives using antenna coefficients given by $\{\mathbf{u}_{-1}, \mathbf{u}_0, \mathbf{u}_1\}$ [see (11)].

The beam-spoiled pattern is generated with weightings such that $\mathbf{v}$ and $\mathbf{r}$ have elements given by

$$\exp\left(2\pi\jmath\frac{2L}{\lambda}\sin\frac{\lambda}{L}(x_k - \bar{x})^2\right) \tag{29}$$

where $\bar{x} = 1/N\sum_{k=1}^{N} x_k$.

1) Transmit Pattern: The transmit condition number[2] is 1.013 showing that the total transmitted power is practically invariant to any phase-only weighting applied to the array. Fig. 4 captures the average transmitted power over three pulses, illustrating how the antenna illuminates the scene over azimuth. The effect of the phase spoil is to slightly squeeze and raise the first sidelobes to a level close to the main lobe, giving the appearance of shoulders adjacent to the original peak. For comparison, the average power of a cyclic three-beam system is plotted showing a lower peak-power but a higher integrated power of 0.4 dB over $\pm 7°$.

2) Two-Way Pattern: Even though the total transmitted power is the same in both cases, when the two-way patterns are computed, one observes a 4.4-dB increase in power when the three-beam system is used versus the beam-spoiled system. This increase in SNR recommends the beam diverse system over the beam-spoiled system. A nondiagonal impedance matrix would change the results further. If the cross-coupling is not accounted for, both the quadratic phase spoil approach and the three-beam approach would change according to (20).

[2]The condition number is defined as $\max\varsigma_k / \min\varsigma_k$.

III. GENERALIZED BEAM-SWITCHED SAR SIGNAL PROCESSING

A. Single-Channel Burst Mode Collection Signal Model

Systems that can change beams (transmit and receive array patterns) from pulse to pulse require little modification to signal-processing algorithms to create high-resolution, high-sensitivity imagery. To set the stage for a multichannel, burst-mode, beam-switched system, this section introduces a single-channel system that can only change beams after every N_1 pulses. Fig. 5 illustrates an example for a two-beam system where f_p represents the PRF and v_a the radar platform speed. Transmit and receive patterns are combined as $\mathcal{F}_k(u) = \mathcal{F}_{T_k}(u)\mathcal{F}_{R_k}(u)$. Since the beams share a common elevation pointing orientation, there is no need to modify the echo window timing, as common with ScanSAR where different beams point to different elevations. For this reason, all pulses can be captured even as the beams transition. In systems where multiple pulses may be in flight at any given time, the receive pattern should be timed to change only when the transmit pulses from the new transmit beam return to the radar. The set of samples from beam 1 and beam 2 can be grouped into a sequence of length $2N_1$.

B. Multichannel Burst-Mode Beam-Switched Signal Model

To adequately sample a time-multiplexed-beam measurement, the PRF employed by a single channel system needs to be accordingly increased leading to a reduction in the measurable swath-width.[3] To avoid the problem of a reduction in swath-width, this section introduces a multichannel system with digital beam forming on receive that can operate at lower PRF settings.

An example of the sampling configuration for a two-channel system measuring two different beams is provided in Fig. 6. In the figure channels, one and two correspond to a beam steered to a Doppler centroid of -400 Hz, while channels three and four represent a beam steered to a Doppler centroid of +400 Hz. At a given range, an N_c-channel (a multichannel receive system such as RADARSAT-2, TerraSAR-X, and ALOS-PALSAR) SAR signal may be represented by the vector quantities

$$\mathbf{y}(n) = \mathbf{s}(n) + \boldsymbol{\nu}(n) \tag{30}$$

where slow time pulse index is given by n, the signal or clutter measurement is given by $\mathbf{s}(n)$, and there is additional "white" noise at each pulse given by $\boldsymbol{\nu}(n) \sim N_{\mathcal{C}}(\mathbf{0}, \mathbf{R}_n = \sigma_n^2\mathbf{I})$. One may consider a set of N_1N_B of such vector measurements,

[3]More strictly speaking, the PRF needs to be increased to a value that can adequately sample the Doppler bandwidth spanned by the union of all beams utilized. In particular, if the beams all point in the same direction, then the PRF does not need to be increased.

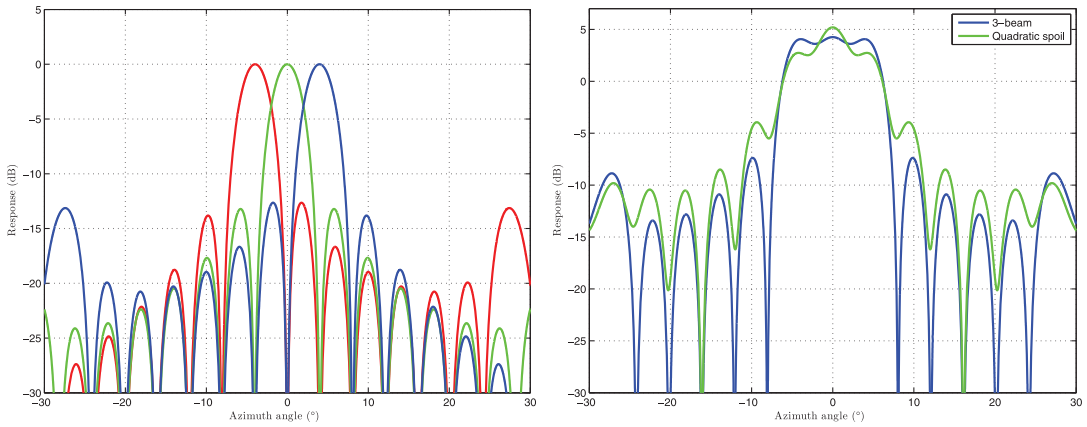

Fig. 4. Normalized three-beam patterns (left) and unormalized quadratically spoiled (phase only) beam pattern compared to average of three-beam pattern (right).

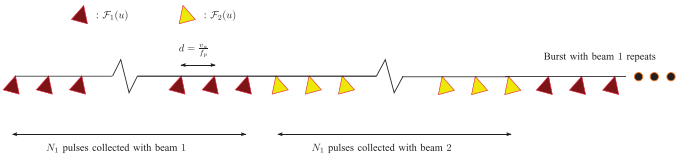

Fig. 5. Two-beam illustration.

as alluded to in Fig. 5, and concatenate the sequence of these vectors into a single long-column vector

$$\mathbf{y}_b(n) = \mathbf{s}_b(n) + \boldsymbol{\nu}_b(n). \tag{31}$$

In the above, $\boldsymbol{\nu}_b(n) \sim N_{\mathcal{C}}(\mathbf{0}, \mathbf{R}_{b_n} = \sigma_n^2 \mathbf{I}_b)$ where $\mathbf{R}_{b_n}$ is an $N_c N_1 N_B \times N_c N_1 N_B$ diagonal matrix. The unambiguous slow-time frequency domain representation of the combination of the sampling delays and antennas used to measure the scene with this concatenated vector may be represented by the vector

$$\mathbf{g}(\omega) = \begin{bmatrix} e^{-\jmath \frac{0 \cdot N_1}{f_p}\omega} \mathbf{d}(\omega) \otimes \boldsymbol{\mathcal{F}}_1[u(\omega)] \\ e^{-\jmath \frac{1 \cdot N_1}{f_p}\omega} \mathbf{d}(\omega) \otimes \boldsymbol{\mathcal{F}}_2[u(\omega)] \\ \vdots \\ e^{-\jmath \frac{(N_B-1) \cdot N_1}{f_p}\omega} \mathbf{d}(\omega) \otimes \boldsymbol{\mathcal{F}}_{N_B}[u(\omega)] \end{bmatrix} \tag{32}$$

where $\otimes$ denotes the Kronecker product

$$\mathbf{d}(\omega) = \begin{bmatrix} e^{-\jmath \frac{0}{f_p}\omega} \\ e^{-\jmath \frac{1}{f_p}\omega} \\ \vdots \\ e^{-\jmath \frac{N_1}{f_p}\omega} \end{bmatrix} \tag{33}$$

and

$$u(\omega) = -\frac{\lambda \omega}{4\pi v_a} \tag{34}$$

and $\boldsymbol{\mathcal{F}}_k[u(\omega)]$ is a vector containing the multichannel measurements with beams rotated in the azimuth direction by an angle in some set indexed by k. The vector of channels measured with

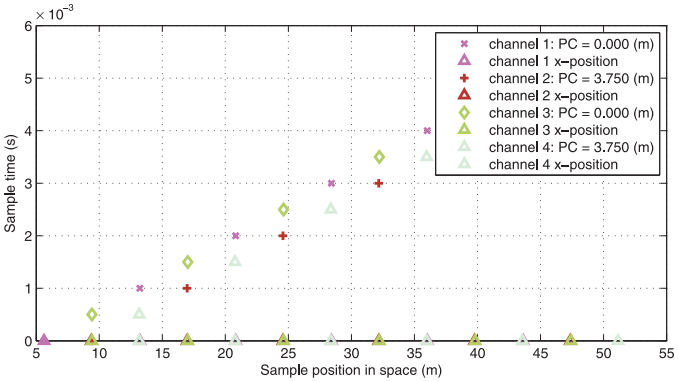

Fig. 6. Two-channel two-beam sampling configuration. Channels one and two correspond to a beam steered to a Doppler centroid of -400 Hz while channels three and four represent a beam steered to a Doppler centroid of +400 Hz. PC stands for phase center position in the antenna coordinate system.

$\mathbf{g}(\omega)$ are sampled at a rate given by $\bar{\omega}_p = 2\pi f_p/(N_B N_1)$, and we define $\mathbf{g}_k(\omega) = \mathbf{g}(\omega + \bar{\omega}_p)$. One may rewrite $\mathbf{g}_k(\omega)$ as

$$\mathbf{g}_k(\omega) = \Phi_k(\omega)\hat{\mathbf{g}}_k(\omega) \tag{35}$$

where

$$\Phi_k(\omega) = \sqrt{\mathbf{g}^\dagger{}_k(\omega)\mathbf{g}_k(\omega)}. \tag{36}$$

The slow-time frequency domain representation of the measured, back-folded signal is then compactly represented by

$$\begin{aligned} \mathbf{y}_b(\omega) &= \sum_k \alpha(\omega + \bar{\omega}_p) e^{\jmath\Omega(\omega + k\bar{\omega}_p)} \Phi_k(\omega)\hat{\mathbf{g}}_k(\omega) + \boldsymbol{\nu}_b(\omega) \\ &= \sum_k y_k \Phi_k(\omega)\hat{\mathbf{g}}_k(\omega) + \boldsymbol{\nu}_b(\omega) \end{aligned} \tag{37}$$

where $\alpha(\omega)$ represents the random process describing terrain reflectivity and $\Omega(\omega)$ represents the azimuth chirp function [6] (both in the slow-time frequency domain).

TABLE II
SIMULATION PARAMETERS

Pulse bandwidth	100 MHz
Pulse length	42 μs
System temperature	297 K
RCS, σ	1 m^2
λ	0.054 m
d	0.9375 m
Near range	1164 km
Satellite velocity	7545 m/s
Effective velocity	7072 m/s

C. Processing Procedure

Methods developed in [6] can be applied to (37) to reconstruct the unambiguous signal. To summarize [6], the objective is to devise processing filters $\mathbf{v}_k(\omega)$

$$y(\omega + k\omega_p) = \mathbf{v}_k^\dagger(\omega)\mathbf{y}_b(\omega) \tag{38}$$

such that the inverse Fourier transform $\mathrm{F}^{-1}\{y(\omega)\exp(-\jmath\Omega(\omega))\}$ over the extended Doppler bandwidth, yields the desired "unfolded" azimuth compressed clutter clutter signal.

This paper adopts the optimum blended minimum mean-square-error (MMSE) solution

$$\begin{aligned} k_k^{\mathrm{opt}}(\omega) &= \varrho\,\sigma_c^2|\Phi_k(\omega)|^2\mathbf{R}_\varrho^{-1}(\omega)\mathbf{g}_k(\omega) \\ &= |\Phi_k(\omega)|^2\hat{\mathbf{R}}_\varrho^{-1}(\omega)\mathbf{g}_k(\omega) \end{aligned} \tag{39}$$

where

$$\begin{aligned} \hat{\mathbf{R}}_\varrho(\omega) &= \hat{\mathbf{R}}_c(\omega) + \frac{(1-\varrho)}{\varrho}\frac{\mathbf{R}_{b_n}(\omega)}{\sigma_c^2} \\ \hat{\mathbf{R}}_c(\omega) &= \mathbf{R}_c(\omega)/\sigma_c^2 = \sum_k |\Phi_k(\omega)|^2\mathbf{g}_k(\omega)\mathbf{g}_k^\dagger(\omega) \end{aligned} \tag{40}$$

and $\mathcal{E}\{|\alpha(\omega)|^2\} = \sigma_c^2$. The parameter $\varrho \in (0, 1]$ allows modification of the reconstructed signal so that for values close to 1, the reconstructed signal will be free of azimuth ambiguities (or grating lobes) to the best possible degree. As shown in [6], this choice corresponds to the projection method proposed in [4] and [5] and, along with certain choices for f_p and the beam directions, can lead to a large reduction in the SNR [7]. Choosing ϱ close to zero, on the other hand, less aggressively eliminates ambiguities, but at the same time maintains the SNR.

IV. SIMULATION OF DATA

Table II lists the common parameters used for all simulations. They reflect the geometry and collection configuration that could be used by a system such as RADARSAT-2. It should be noted that this simulation is constructed for an ideal system. Practical issues such as Doppler centroid deviation and multiplicative phase-noise effects are deferred for future work, should such a system be utilized.

The benchmark simulation, to which all beam switching simulations are compared, generates image characteristics for one of the Ultra-Fine modes of RADARSAT-2; see Table III. As discussed in [9], this mode uses a phase-spoiled beam in azimuth and collects using a dual-channel configuration. The relevant image characteristics of this mode are listed in Table III.

TABLE III
SIMULATION BENCHMARK FROM ULTRA FINE MODE

PRF (Hz)	N_1	SNR (dB)	PAR (dB)	ISLR (dB)	3 dB res (m)
1600	1	26.09	–24.64	–16.25	2.55

A. Three-Beam Full-Antenna Mode

Simulation results for a three-beam mode at two different burst lengths are shown in Table IV. As seen, the 3-dB resolution is comparable to the benchmark. For the PRF selected, one expects an SNR gain on the order of $3000/1600 = 2.7$ dB with respect to the benchmark mode. The SNR gain in the first row of the table, however, is about 3.3 dB higher. The real gain here is that similar image characteristics to the benchmark mode are achieved with a single aperture system, albeit at the expense of a narrower swath due to the increased PRF. As one reads down the table, the resolution widens to about 3.0 m; however, the SNR improves to about 4.0 dB over the benchmark. The lower rows in the table also show that the ambiguities start to rise quickly and the integrated sidelobe ratio increases as well.

B. Two-Beam Dual-Antenna Receive

This section simulates a two-beam mode using a dual-channel approach that differs from the benchmark mode in that all columns are used on receive. Figures generated for $N_1 = 1$ and $N_1 = 2$ are tabulated in Table V. As can be seen, for $N_1 = 1$, the 3-dB resolution is on the order of 3 m. The SNR, on the other hand, is improved over the benchmark mode by up to 2 dB. A comparable mode $N_1 = 2$ uses $\varrho = 10^{-7}$; however, all image characteristics are poorer than the benchmark mode. This demonstrates that although it is possible to process the bursted type of signal, image quality degrades rapidly.

C. Three-Beam Dual-Antenna Receive

This section demonstrates the capability predicted for a three-beam dual-receive mode. The special choice of 3000 Hz is chosen as it represents uniform spatial sample points for the dual-antenna phase centers. As listed in Table VI, for a resolution of 2 m, the SNR is seen to be 5 dB better than the benchmark mode (2.7 dB is accounted for in the increase in PRF).

D. Five-Beam Dual-Antenna Receive

The final simulations show the performance of a five-beam mode. The first row of Table VII shows that one can achieve a resolution of 1.3 m with such a mode and obtain an SNR about 1 dB better than the benchmark mode. The third row shows that one can achieve a 1.4-m resolution with a 5-dB improvement in the SNR.

TABLE IV
SIMULATION RESULTS FOR FULL-ANTENNA RECEIVE MODE WITH THREE BEAMS

PRF (Hz)	ϱ	N_1	Beams (Hz)	SNR (dB)	PAR (dB)	ISLR (dB)	3dB res (m)
3000	1	1	–750,0,750	29.40	–36.47	–13.61	2.67
3000	10^{-1}	1	–750,0,750	29.40	–36.47	–13.61	2.67
3000	10^{-2}	1	–750,0,750	29.40	–36.47	–13.61	2.67
3000	10^{-7}	2	–750,0,750	24.84	–25.56	–13.38	2.76
3000	10^{-8}	2	–750,0,750	27.73	–16.42	–12.46	2.89
3000	10^{-9}	2	–750,0,750	30.23	–9.97	–10.60	3.00

TABLE V
SIMULATION RESULTS FOR DUAL-ANTENNA RECEIVE MODE WITH TWO BEAMS

PRF (Hz)	ϱ	N_1	Beams (Hz)	SNR (dB)	PAR (dB)	ISLR (dB)	3dB res (m)
1600	10^{-6}	1	–500,500	27.38	–33.33	–14.29	2.90
1600	10^{-7}	1	–500,500	27.98	–32.90	–13.95	2.96
1600	10^{-8}	1	–500,500	28.48	–29.64	–13.00	3.12
1600	10^{-9}	1	–500,500	28.77	–22.39	–10.99	3.36
1600	10^{-6}	2	–500,500	21.88	–27.92	–13.63	2.93
1600	10^{-7}	2	–500,500	25.52	–24.58	–13.55	3.04
1600	10^{-8}	2	–500,500	27.19	–18.58	–13.42	3.19
1600	10^{-9}	2	–500,500	28.54	–12.21	–11.58	3.38

TABLE VI
SIMULATION RESULTS FOR DUAL-ANTENNA RECEIVE MODE WITH THREE BEAMS

PRF (Hz)	ϱ	N_1	Beams (Hz)	SNR (dB)	PAR (dB)	ISLR (dB)	3dB res (m)
3000	10^{-6}	1	–1000,0,1000	30.07	–50.80	–13.12	1.95
3000	10^{-7}	1	–1000,0,1000	31.08	–44.84	–12.74	2.02
3000	10^{-8}	1	–1000,0,1000	31.47	–41.01	–12.08	2.12
3000	10^{-9}	1	–1000,0,1000	31.53	–37.89	–10.76	2.24

TABLE VII
SIMULATION RESULTS FOR DUAL-ANTENNA RECEIVE MODE WITH FIVE BEAMS

PRF (Hz)	ϱ	N_1	Beams (Hz)	SNR (dB)	PAR (dB)	ISLR (dB)	3dB res (m)
3000	10^{-6}	1	–2000,–1000,0,1000,2000	27.75	–43.00	–11.73	1.30
3000	10^{-7}	1	–2000,–1000,0,1000,2000	29.07	–32.89	–11.59	1.31
3000	10^{-8}	1	–2000,–1000,0,1000,2000	30.28	–20.31	–11.13	1.34
3000	10^{-9}	1	–2000,–1000,0,1000,2000	31.23	–12.07	–10.00	1.38
3000	10^{-6}	1	–1500,–750,0,750,1500	28.39	–40.07	–13.76	1.63
3000	10^{-7}	1	–1500,–750,0,750,1500	29.45	–35.64	–13.58	1.65
3000	10^{-8}	1	–1500,–750,0,750,1500	30.46	–22.73	–13.46	1.72
3000	10^{-9}	1	–1500,–750,0,750,1500	31.33	–13.10	–13.48	1.80

V. CONCLUSION

A measurement scheme that uses beam switching can generate high-resolution imagery that has higher sensitivity than an equivalent scheme that uses beam spoiling. If mutual coupling effects between phased-array elements are significant and not accounted for, the SNR can also degrade significantly. A method to process data collected by a system that can beam-switch, including the case when the system is unable to switch beams at the PRF, is presented. The switching of beams in a bursting fashion introduces new grating lobes (equivalent to ambiguities for a lower PRF system) which the new signal processing technique can eliminate; however, reduction in the grating lobes comes at the cost of reduced SNR. The method uses a user-defined parameter to trade SNR against the grating lobes as the user desires. Finally, by collecting data through multiple receive subarrays, this paper shows how the beam-switched signal can be processed to yield higher SNR measurements with reduced grating lobe interference and lower azimuth ambiguity levels than a benchmark Ultra Fine mode on RADARSAT-2.

In summary, a burst length of one yields the best performance, but performance can be improved through the use of a multilpe-channel system, and to a lesser degree, through the use to adapted signal processing. Although the signal processing can eliminate the new grating lobes, the cost is reduced SNR which degrades further as the number of pulses in the burst increases. Further, as the angle between beams increases, the geometrical resultion increases, but the SNR may decrease due to the requirement to manage grating lobes.

Future work will investigate the method developed for burst-mode signal processing to the case of SCANSAR. Further, the authors wish to pursue proof-of-concept experiments both with RADARSAT-2, which cannot switch beams at the PRF, and with systems in the upcoming RCM mission, which may be able to switch beams at the PRF.

Appendix
Eigenvector and Eigenvalue Decomposition

This section computes an eigen representation of $\mathbf{F}$ under certain conditions required to satisfy the Shannon sampling theorem, and also under the assumption that negligible power is transmitted through the antenna back-lobes. The inner product of the lth row of $\mathbf{F}$ and the nth column of the DFT matrix yields

$$\begin{aligned}\phi_l(n) &= \frac{1}{\sqrt{N}}\sum_{k=0}^{N-1} F_{l-k}\exp\left(-\jmath 2\pi\frac{kn}{N}\right)\\ &= \frac{1}{\sqrt{N}}\int_{-1}^{1}|\mathcal{F}_u(u)|^2\exp(-\jmath\beta l du)\\ &\quad\sum_{k=0}^{N-1}\exp\left(\jmath k\left[\beta du - 2\pi\frac{n}{N}\right]\right)\mathrm{d}u. \end{aligned}\tag{41}$$

Consider the function $s(u) = |\mathcal{F}_u(u)|^2$. Assume that the frequency content of $s(u)$ is restricted to $[-B_u/2, B_u/2]$ (here, and in the following, we mean frequency as the dual to the dimensionless variable u). According to the Shannon sampling theorem, if $s(u)$ is sampled adequately, it can be reconstructed from its samples; that is, $s(u)$ can be represented as the windowed inverse Fourier transform of the periodic signal

$$S(f) = \sum_{k=-\infty}^{\infty} s(u_k)\frac{\lambda}{Nd}\exp\left(-\jmath 2\pi u_k f\right)\tag{42}$$

where the sampling frequency across u (which depends on N) is given by

$$f_s = \frac{Nd}{\lambda} > B_u/2\tag{43}$$

and

$$u_k = k\frac{\lambda}{Nd}.\tag{44}$$

Specifically

$$\begin{aligned}s(u) = &\int \mathrm{Rect}\left(\frac{f\lambda}{Nd}\right)\\ &\times\sum_{k=-\infty}^{\infty} s(u_k)\frac{\lambda}{Nd}\exp\left(-\jmath 2\pi u_k f\right)\exp\left(\jmath 2\pi u f\right)\mathrm{d}f\end{aligned}\tag{45}$$

where

$$\mathrm{Rect}(u) = \begin{cases}1, & \text{if } |u| < \frac{1}{2}\\ 0, & \text{otherwise.}\end{cases}\tag{46}$$

With this expression, and assuming that $s(u) = 0$ for $|u| > 1$, which is another way of stating that negligible power is transmitted through the back-lobes [(47), shown at the bottom of this page], where $\delta(k, k')$ is the Kronecker–Delta function. The first two terms of the last line above represent the element of the lth row and nth column of the DFT matrix while the last two terms are independent of l and represent the eigenvalue for the nth column of the DFT matrix. The above analysis is valid so long as N, d, λ are chosen to satisfy (43). This condition depends on the element factor for each antenna element.

$$\begin{aligned}\phi_l(n) &= \frac{1}{\sqrt{N}}\iint\mathrm{Rect}\left(\frac{f\lambda}{Nd}\right)\sum_{k'=-\infty}^{\infty} s(u_{k'})\frac{\lambda}{Nd}\exp\left(-\jmath 2\pi u_{k'} f\right)\exp\left(\jmath 2\pi u f\right)\exp(-\jmath\beta l du)\sum_{k=0}^{N-1}\exp\left(\jmath k\left[\beta du - 2\pi\frac{n}{N}\right]\right)\mathrm{d}f\mathrm{d}u\\ &= \frac{1}{\sqrt{N}}\int\mathrm{Rect}\left(\frac{f\lambda}{Nd}\right)\sum_{k'=-\infty}^{\infty} s(u_{k'})\frac{\lambda}{Nd}\exp\left(-\jmath 2\pi u_{k'} f\right)\sum_{k=0}^{N-1}\exp\left(-2\pi\jmath k\frac{n}{N}\right)\int\exp\left(2\pi\jmath u\left[f - \frac{d}{\lambda}(l-k)\right]\right)\mathrm{d}u\mathrm{d}f\\ &= \frac{1}{\sqrt{N}}\int\mathrm{Rect}\left(\frac{f\lambda}{Nd}\right)\sum_{k'=-\infty}^{\infty} s(u_{k'})\frac{\lambda}{Nd}\sum_{k=0}^{N-1}\exp\left(-\jmath 2\pi u_{k'} f\right)\exp\left(-2\pi\jmath k\frac{n}{N}\right)\delta\left(f - \frac{d}{\lambda}(l-k)\right)\mathrm{d}f\\ &= \frac{1}{\sqrt{N}}\sum_{k'=-\infty}^{\infty} s(u_{k'})\frac{\lambda}{Nd}\sum_{k=0}^{N-1}\mathrm{Rect}\left(\frac{l-k}{N}\right)\exp\left(-\jmath 2\pi u_{k'}\frac{d}{\lambda}(l-k)\right)\exp\left(-2\pi\jmath u_{k'}\frac{d}{\lambda}(l-k)\right)\exp\left(-2\pi\jmath k\frac{n}{N}\right)\\ &= \frac{1}{\sqrt{N}}\sum_{k'=-\infty}^{\infty} s(u_{k'})\frac{\lambda}{Nd}\exp\left(-\jmath 2\pi n\frac{l}{N}\right)\sum_{k=0}^{N-1}\mathrm{Rect}\left(\frac{l-k}{N}\right)\exp\left(-\jmath 2\pi k'\frac{(l-k)}{N}\right)\exp\left(\jmath 2\pi n\frac{(l-k)}{N}\right)\\ &= \frac{1}{\sqrt{N}}\exp\left(-\jmath 2\pi n\frac{l}{N}\right)\frac{\lambda}{d}\sum_{k'=-\infty}^{\infty} s(u_{k'})\delta(n+mN, k') = \frac{1}{\sqrt{N}}\exp\left(-\jmath 2\pi n\frac{l}{N}\right)\frac{\lambda}{d}\sum_{m=-\infty}^{\infty} s(u_{n+mN})\\ &= \frac{1}{\sqrt{N}}\exp\left(-\jmath 2\pi n\frac{l}{N}\right)\frac{\lambda}{d}\sum_{m}\left|\mathcal{F}_u\left(\frac{\lambda[n+mN]}{Nd}\right)\right|^2\end{aligned}\tag{47}$$

ACKNOWLEDGMENT

The authors would like to thank Mr. T. Laneve for his discussions and demonstrations of element coupling effects on phased-array radars and Mr. K. James for his discussions on the RADARSAT-2 Ultra-Fine beam mode.

REFERENCES

[1] M. Skolnik, *Radar Handbook*. New York, NY, USA: McGraw-Hill, 1990.
[2] I. G. Cumming and F. H. Wong, *Digital Processing of Synthetic Aperture Radar Data: Algorithms and Implementation*. Norwood, MA, USA: Artech House, 2005.
[3] C. V. Jakowatz, D. E. Wahl, P. H. Eichel, D. C. Ghiglia, and P. A. Thopmson, *Spotlight-Mode Synthetic Aperture Radar: A Signal Processing Approach*. Boston, MA, USA: Kluwer, 1996.
[4] N. Gebert, G. Krieger, and A. Moreira, "Digital beamforming on receive: Techniques and optimization strategies for high-resolution wide-swath SAR imaging," *IEEE Trans. Aerosp. Electron. Syst.*, vol. 45, no. 2, pp. 564–592, Apr. 2009.
[5] G. Krieger, N. Gebert, and A. Moreira, "Unambiguous SAR signal reconstruction from nonuniform displaced phase center sampling," *IEEE Geosci. Remote Sens. Lett.*, vol. 1, no. 4, pp. 260–264, Oct. 2004.
[6] I. Sikaneta, C. Gierull, and D. Cerutti-Maori, "Optimum signal processing for multichannel SAR: With application to high-resolution wide-swath imaging," *IEEE Trans. Geosci. Remote Sens.*, vol. 52, no. 10, pp. 6095–6109, Oct. 2014.
[7] D. Cerutti-Maori, I. Sikaneta, J. Klare, and C. Gierull, "MIMO SAR processing for multichannel high-resolution wide-swath radars," *IEEE Trans. Geosci. Remote Sens.*, vol. 52, no. 8, pp. 5034–5055, Aug. 2014.
[8] Z. Li, H. Wang, T. Su, and Z. Bao, "Generation of wide-swath and high-resolution SAR images from multichannel small spaceborne SAR systems," *IEEE Geosci. Remote Sens. Lett.*, vol. 2, no. 1, pp. 82–86, Jan. 2005.
[9] P. A. Fox, A. P. Luscombe, and A. A. Thompson, "RADARSAT-2 SAR modes development and utilization," *Can. J. Remote Sens.*, vol. 30, no. 3, pp. 258–264, 2004.
[10] P. Hannan, "The element-gain paradox for a phased-array antenna," *IEEE Trans. Antennas Propag.*, vol. 12, no. 4, pp. 423–433, Jul. 1964.
[11] J. Allen, "Gain and impedance variation in scanned dipole arrays," *IRE Trans. Antennas Propag.*, vol. 10, no. 5, pp. 566–572, Sep. 1962.
[12] D. Calabrese, "Discrete stepped strip (DI2S)," in *Proc. 10th Eur. Conf. Synth. Aperture Radar*, Jun. 2014, pp. 1–4.
[13] J. Mittermayer, S. Wollstadt, P. Prats-Iraola, P. Lopez-Dekker, G. Krieger, and A. Moreira, "Bidirectional SAR imaging mode," *IEEE Trans. Geosci. Remote Sens.*, vol. 51, no. 1, pp. 601–614, Jan. 2013.
[14] J. H. G. Ender, "The meaning of k-space for classical and advanced SAR techniques," in *Proc. Int. Symp. Phys. Signal Image Process. (PSIP'01)*, Marseille France, Jan. 2001, pp. 23–38.
[15] M. Skolnik, *Radar Handbook*. New York, NY, USA: McGraw-Hill, 1990.

Ishuwa Sikaneta, photograph and biography not available at the time of publication.

Christoph Gierull, photograph and biography not available at the time of publication.

DOCUMENT CONTROL DATA

(Security markings for the title, abstract and indexing annotation must be entered when the document is Classified or Designated)

1. ORIGINATOR (The name and address of the organization preparing the document. Organizations for whom the document was prepared, e.g., Centre sponsoring a contractor's report, or tasking agency, are entered in Section 8.)

DRDC – Ottawa Research Centre
Defence Research and Development Canada
3701 Carling Avenue
Ottawa, Ontario K1A 0Z4
Canada

2a. SECURITY MARKING (Overall security marking of the document including special supplemental markings if applicable.)

CAN UNCLASSIFIED

2b. CONTROLLED GOODS

NON-CONTROLLED GOODS
DMC A

3. TITLE (The complete document title as indicated on the title page. Its classification should be indicated by the appropriate abbreviation (S, C or U) in parentheses after the title.)

Phased-Array Beam-Diversity with Multiple Channels for Improved SAR Imaging

4. AUTHORS (last name, followed by initials – ranks, titles, etc., not to be used)

Sikaneta, Ishuwa; Gierull, Christoph;

5. DATE OF PUBLICATION (Month and year of publication of document.)	6a. NO. OF PAGES (Total containing information, including Annexes, Appendices, etc.)	6b. NO. OF REFS (Total cited in document.)
November 2017	10	15

7. DESCRIPTIVE NOTES (The category of the document, e.g., technical report, technical note or memorandum. If appropriate, enter the type of report, e.g., interim, progress, summary, annual or final. Give the inclusive dates when a specific reporting period is covered.)

External Literature (P)

8. SPONSORING ACTIVITY (The name of the department project office or laboratory sponsoring the research and development – include address.)

DRDC – Ottawa Research Centre
Defence Research and Development Canada
3701 Carling Avenue
Ottawa, Ontario K1A 0Z4
Canada

9a. PROJECT OR GRANT NO. (If appropriate, the applicable research and development project or grant number under which the document was written. Please specify whether project or grant.)	9b. CONTRACT NO. (If appropriate, the applicable number under which the document was written.)

10a. ORIGINATOR'S DOCUMENT NUMBER (The official document number by which the document is identified by the originating activity. This number must be unique to this document.)	10b. OTHER DOCUMENT NO(s). (Any other numbers which may be assigned this document either by the originator or by the sponsor.)
DRDC-RDDC-2017-P114	

11a. FUTURE DISTRIBUTION (Any limitations on further dissemination of the document, other than those imposed by security classification.)

Public release

11b. FUTURE DISTRIBUTION OUTSIDE CANADA (Any limitations on further dissemination of the document, other than those imposed by security classification.)

12. ABSTRACT (A brief and factual summary of the document. It may also appear elsewhere in the body of the document itself. It is highly desirable that the abstract of classified documents be unclassified. Each paragraph of the abstract shall begin with an indication of the security classification of the information in the paragraph (unless the document itself is unclassified) represented as (S), (C), (R), or (U). It is not necessary to include here abstracts in both official languages unless the text is bilingual.)

This paper discusses the ability of a SAR to create high-resolution images with high sensitivity in a stripmap configuration. Since geometric resolution is driven by the effective azimuth beamwidth of the antenna, it compares beam spoiling methods to beam switching methods with particular attention to the achieved SNR. It also formulates the effects of element mutual coupling on the SNR. Further, since existing systems may not be able to switch beams at a rate equivalent to the PRF, this paper also discusses a method to process beam switched data collected in a burst configuration, showing that SNR and the presence of grating lobes trade against each other as the number of pulses per burst increases. Finally, this paper investigates improvements to signal quality offered by using a multichannel system, with elements aligned in the flight direction, over a single channel system.

13. KEYWORDS, DESCRIPTORS or IDENTIFIERS (Technically meaningful terms or short phrases that characterize a document and could be helpful in cataloguing the document. They should be selected so that no security classification is required. Identifiers, such as equipment model designation, trade name, military project code name, geographic location may also be included. If possible keywords should be selected from a published thesaurus, e.g., Thesaurus of Engineering and Scientific Terms (TEST) and that thesaurus identified. If it is not possible to select indexing terms which are Unclassified, the classification of each should be indicated as with the title.)

RADARSAT-2, space-based SAR, resolution, High Resolution Wide Swath, Mutual Coupling, Radar Antennas